Modeling the Reaction Mechanism of Membrane Penetration by Striated Amphiphitic Gold Nanoparticles

by

Reid Chi Van Lehn

Submitted to the Department of Materials
Science and Engineering in Partial
Fulfillment of the Requirements for the
Degree of

Bachelor of Science

at the

Massachusetts Institute of Technology

May 2009
[June 2009]

Signature of Author..
Department of Materials Science and Engineering
May 15, 2009

Certified by ....
Alfredo Alexander-Katz
Toyota Career Development Assistant Professor of Materials Science and Engineering
Thesis Supervisor

Accepted by ....
Lionel C. Kimerling
Professor of Materials Science and Engineering
Chair, Undergraduate Committee

Modeling the Reaction Mechanism of Membrane Penetration by Striated Amphiphitic Gold Nanoparticles

by

Reid Chi Van Lehn

Submitted to the Department of Materials Science and Engineering
on May 15th, 2009
in Partial Fulfillment of the Requirements for the
Degree of Bachelor of Science

Abstract

The desire to desire targeted drug delivery devices capable of releasing therapeutic payloads within the cytosol of cells has led to research on nanoparticles as suitable drug carriers. Recently, it was shown that gold nanoparticles coated in striped, alternating layers of hydrophobic and hydrophilic ligands are capable of non-disruptively penetrating a lipid bilayer, a discovery with potential implications in drug delivery. While the reaction mechanism is not known, initial experimental results indicate that endocytosis and membrane poration could be ruled as possible mechanisms. In this work, we explore the reaction mechanism of membrane penetration using a coarse-grained Brownian Dynamics model. We also define a Monte Carlo simulation for modeling ligand motion on the nanoparticle surface based on a single order parameter, and describe a method for approximating the interaction energy with the bilayer as a function of this parameter. Our simulations demonstrate the dependence of nanoparticles penetration on the surface mobility, not explicit conformation, of coated ligands. They demonstrate that while nanoparticles with static ligands in a striped conformation are unable to penetrate the bilayer, enabling surface mobility allows penetration by the induced formation of a small, transient pore of a comparable size to the nanoparticle. Our results offer an enhanced understanding of the nanoparticles-bilayer interaction and an identification of the property necessary for membrane penetration.

Thesis Supervisor: Alfredo Alexander-Katz

Title: Toyota Career Development Assistant Professor of Materials Science and Engineering

TABLE OF CONTENTS

LIST OF FIGURES

CHAPTER 1: Introduction

The development of nanoscale materials for drug delivery is an important current topic in materials science. The goal of targeted drug delivery systems is to release therapeutic agents within specific cells without risking drug toxicity, a goal that requires biocompatible or biodegradable delivery devices[1]. Targeted drug delivery systems using nanoparticles as drug carriers are being investigated as a more effective means of combating cancer and other diseases[2]. A new advance in this research has recently been made by the synthesis of nanoparticles coated with alternating ribbon-like domains of hydrophobic and hydrophilic particles[3]. In a recent study, it was found that these particles were capable of penetrating the cellular membrane without any evidence of bilayer disruption, and without being trapped in endosomal compartments[4]. This ability enables the particles to access the cytosol of target cells without becoming entrapped by cellular machinery, making these particles suitable as potential efficient drug carriers[5]. The same study found that identical nanoparticles coated with randomly ordered domains of the same hydrophobic and hydrophilic materials were largely found trapped in endosomes rather than freely penetrating the lipid bilayer, indicating the importance of order in membrane penetration.

Though experimental evidence has demonstrated the behavioral difference between nanoparticles with ordered and unordered surface conformations, no mechanism has yet been proposed to explain the observed differences. Understanding the reaction mechanism of bilayer penetration will enable more accurate tuning of the nanoparticle surface properties to ensure penetration, and may enable penetration of the more complex nuclear membrane[6]. Previously identified reaction mechanisms for particle uptake include endocytosis[7] and membrane poration[8]. Endocytosis and other transport mechanism were eliminated as a possible mechanism of particle uptake by the observation of membrane penetration despite the application of endocytic inhibitors and at low temperatures[9]. Furthermore, while previous studies have shown that cationic nanoparticles can penetrate the bilayer by membrane poration[10] at the expense of cytotoxicity[11], this mechanism was also eliminated by the observation of no cytosol leakage during penetration[4]. It has thus been proposed that membrane disruption is tied to fusion with the nanoparticle by a mechanism related to the striated conformation[4].

We propose that nanoparticle penetration is dependent on the surface mobility of the nanoparticle ligands, not the actual conformation of beads on the surface. It is currently believed that the surface properties of the nanoparticle are controlled by an entropic mechanism dependent upon the relative lengths of the hydrophobic and hydrophilic ligands, and that phase properties on the surface can be controlled by altering the properties of these surface proteins[12]. Given that the mechanism is primarily entropic, the influence of additional electrostatic interactions with the bilayer could lead to widespread rearrangement of ligands on the surface of the nanoparticle; for example, hydrophilic ligands may rearrange to positions on the surface closer to the hydrophilic head region of the bilayer. The specific mobility of the ligands under the influence of an external interaction with the bilayer would then be correlated with the phase separation characteristics. If phase separation is preferred, then ligands on the surface may have difficulty moving through phases on the surface in response to external potentials; if mixing is preferred, then ligands on the nanoparticle may not cluster near the interface with a bilayer. As there is no strong energetic preference for either mixing or phase separation, the formation of striped phases may imply that surface mobility is easy when exposed to external interactions, allowing the striped phases to form entropically.

It is thus proposed that surface mobility and the realignment of ligands on the nanoparticle surface is the primary cause of nanoparticle penetration, and that the observed failure of nanoparticles coated either randomly or in distinct phases to penetrate the bilayer is explained by lower ligand mobility. Penetration could occur by the disruption of the bilayer by electrostatic or Van or Waals interactions with the nanoparticle leading to the rearrangement of ligands on the surface to stabilize the bilayer-nanoparticle complex. To test this hypothesis, we first sought to identify the surface properties of the nanoparticles that would best encourage membrane penetration. We developed a model for ligand motion on the nanoparticles surface using a Monte Carlo algorithm, and incorporated bilayer interaction by treating the bilayer as a static field that biased the movement of ligand beads. This "ghost membrane" simulation served to identify the surface characteristics most favorable for bilayer penetration. Next, we modeled the spontaneous passage of the nanoparticle through the bilayer with a coarse-grained Brownian Dynamics simulation to directly predict the reaction mechanism. Together, these two separate simulations provide an understanding of the reaction mechanism and essential parameters governing nanoparticle penetration.

CHAPTER 2: Nanoparticle Simulations

I. INTRODUCTION

Our initial hypothesis regarding the mechanism of membrane penetration assumed that this ability depends highly upon the reorganization of ligands on the nanoparticle's surface. A first goal was to derive the interaction energy between the bilayer and nanoparticles as a function of the nanoparticle's position during bilayer penetration. This energy landscape would be derived by treating the bilayer as a static field that interacts with a nanoparticle being moved in discrete steps to different positions within field. By ignoring the complexity inherent in a full simulation of the nanoparticle and bilayer, a simple energy landscape could be developed, permitting an analysis of the likely barriers to penetration facing the nanoparticle, and illustrating the correlation between ligand surface mobility and the energy barrier to penetration. The coarse-grained simulation outlined in Chapter 3 could then be tuned by further identification of the parameters responsible for membrane penetration.

II. METHODS

A. Nanoparticle assembly

A first necessity of this model was to assemble a nanoparticle at a lengthscale appropriate for analysis. A coarse-grained model was chosen such that the nanoparticle was composed of a number of beads, each of which represented a diameter of 6 Å, or approximately the width of each striped domain from the experimental study[4]. Given that the nanoparticles used in the experimental procedure were 5 nm in diameter, the nanoparticle was assembled such that it was 10 beads in diameter. The nanoparticle was assembled as a hollow shell to prevent needless computation; this required 273 beads.

Beads were assigned to be either "hydrophilic" or "hydrophobic" in character to mimic the formation of surface domains. Aside from this difference, beads were identical in all respects, and the atomic scale entropy differences were ignored. No attempt was made to model the self-assembly of striped domains; instead, beads were simply assigned values randomly for this experiment. Figure 1 illustrates an assembled nanoparticle with randomly distributed beads of both types.

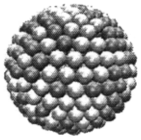

Figure 1: Assembled nanoparticle; white beads are hydrophilic, blue are hydrophobic

B. Monte Carlo algorithm for controlling ligand surface mobility

A Monte Carlo algorithm was developed to control the exchange of beads on the surface of the nanoparticle, representing the movement of ligands on the surface. A model for bead-bead interactions on the particle surface was inspired by the Ising model[13] for magnetic systems, which gives system energy of like form:

$$E_S = -J_q \sum_{j \in n(i)} s_i s_j - \mu_B B \sum_i s_i$$

where J_q is the strength of interactions between spins, q is the number of interacting neighbors, s_i is the spin (given as ± 1) of a particle *i*, and *n(i)* denotes the set of neighbors of bead *i*. For the nanoparticle system, bead type (hydrophobic or hydrophilic) is analogous to spin and bilayer interaction is analogous to the external magnetic field. The chief difference between the two models is in separately defining ε_S for the energy of interaction between beads of the same type and ε_D for the interaction of beads of different type, rather than a single parameter J_q.

The Monte Carlo algorithm was then defined as follows:

1) Choose random bead *i* such that $i \in \mathit{all\ nanoparticle\ beads}$
2) Choose random bead *j* such that $j \in n(i)$; note that near-neighbors are defined as being within a prescribed cutoff distance approximately equivalent to 1 bead diameter, defined such that the average number of near-neighbors per bead is 4. To ensure the conservation of each bead type, the type of bead *j* must be different than that of bead *i*.
3) Compute total energy of interaction between beads *i*,*j* and all near-neighbors, such that

   $$E_{ij} = \sum_{i \neq k} \varepsilon(i,k) + \sum_{j \neq l} \varepsilon(j,l)$$

   where *k*, *l* are the indices of near-neighbors of bead *i* and *j* respectively, and

   $\varepsilon(i,j) = \varepsilon_S, \varepsilon_D$ if the two beads are the same or different respectively.
4) Compute total energy of interaction between beads *i*,*j* and all near-neighbors as if beads *i* and *j* had switched places; that is, changed types. This gives:

   $$E_{ji} = \sum_{j \neq k} \varepsilon(j,k) + \sum_{i \neq l} \varepsilon(i,l)$$
5) Compute the total energy change associate with switching beads *i* and *j* by subtracting the result of step 3 from step 4.

   $$\Delta E_{ij} = \sum_{j \neq k} \varepsilon(j,k) + \sum_{i \neq l} \varepsilon(i,l) - \sum_{i \neq k} \varepsilon(i,k) + \sum_{j \neq l} \varepsilon(j,l)$$

   $$\Delta E_{ij} = (E_{il} + E_{jk}) - (E_{ik} + E_{jl})$$

   If $\Delta E_{ij} \leq 0$ then the switch is retained and bead *i* and bead *j* switch types (note that the indices essentially refer to a position on the surface of the nanoparticle so that only the hydrophilic or –phobic type of the position changes). If $\Delta E_{ij} > 0$, then retain change with probability $e^{-\Delta E_{ij}/kT}$.

An illustration of the basic algorithm is given in Figure 2.

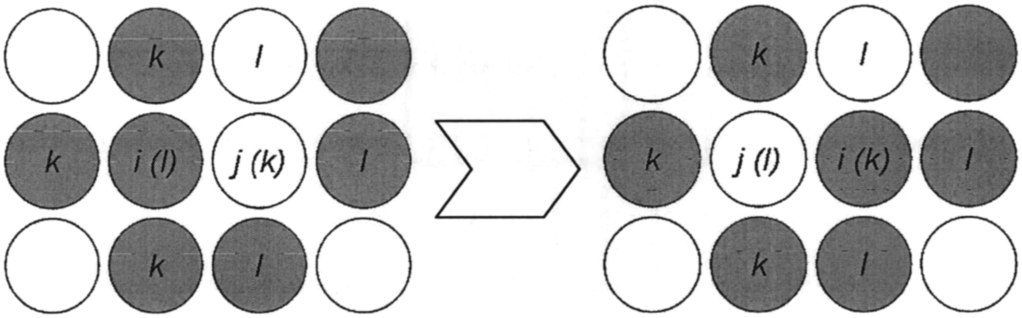

Figure 2: Illustration of energy change in attempted MC timestep; energy of first state (on left) between bead *i* and neighbors *k* and between bead *j* and neighbors *l* is $4\varepsilon_D + 4\varepsilon_S$; energy of second state (on right) between bead *j* and neighbors *k* and bead *i* and neighbors *l* is $6\varepsilon_D + 2\varepsilon_S$; hence $\Delta E_{ij} = 2\varepsilon_D - 2\varepsilon_S$.

C. Nanoparticle Phase Diagram

Based on the Monte Carlo algorithm outlined above, it was thus expected that the phase separation behavior of ligands on the surface of the nanoparticle would be governed primarily by the relationship between ε_S and ε_D, which was explored by holding $\varepsilon_S = 1.0$ and varying ε_D. For simplicity, ε_D will be renamed as ε. The expectation was that low values of ε would promote random mixing while high values would promote phase separation. To calculate the value of ε that causes a phase transition, the Monte Carlo algorithm was allowed to run for 10^7 timesteps, with the total energy of the system calculated every 10,000 steps after the system's energy equilibrated. The specific heat of the system was then approximated via

$$C_V \propto \frac{1}{N}\sum_{i=0}^{N}(E_i - \overline{E})^2$$

where N is the total number of points sampled and E_i is the total energy of the system (based on near-neighbor energy interactions) at a given point[14]. The phase transition was then determined from the peak in the graph of C_V versus ε.

D. "Ghost Membrane"

To determine the energy landscape as the nanoparticle traversed a membrane, a so-called "ghost membrane" technique was employed. Rather than define a fully-interacting membrane, regions along the z-axis were defined corresponding to the hydrophilic head regions and hydrophobic tail region of the membrane, with length scales chosen analogous to physical systems. The nanoparticle was then moved in discrete leaps along the z-axis, thereby passing through the regions designated as the membrane. An interaction parameter ε_B governing the energy of interaction between a nanoparticle bead and a region of the same or different type was then defined. As the nanoparticle was moved down the z-axis of the simulation box (with the bilayer spanning the xy-plane), this parameter contributed a negative energy of interaction to the Monte Carlo calculation when a bead was in a region of related type (e.g. a hydrophilic bead in the head region) and a positive energy of interaction when the bead was in a region of unrelated type (e.g. a hydrophilic bead in the tail region). The complete energy of the system before and after a potential Monte Carlo switch thus included both the energy of interaction with all of a bead's near-neighbors and the energy of interaction with the bilayer, changing the equation to:

$$E_{ij} = \sum_{i \neq k} \varepsilon(i, k) + \sum_{j \neq l} \varepsilon(j, l) + \varepsilon_B(i) + \varepsilon_B(j)$$

Hence, the inclusion of the bilayer interaction weighted the movement of nanoparticle beads to positions such that bilayer interaction was maximized. Using this "ghost membrane" construction, it was thus possible to plot the overall energy of the nanoparticle as a function of position as the nanoparticle traversed the bilayer.

III. RESULTS AND DISCUSSION

A. Phase Diagram

Plotting the specific heat of the nanoparticle system in the absence of bilayer interactions as a function of primary tuning parameter $\varepsilon = \varepsilon_D$ showed clear, distinct peaks near the phase transition as expected. Figure 3 shows a comparison of graphs for different values of the volume fraction Φ. As expected, the graphs are roughly the same between values of Φ symmetric about $\Phi = 0.5$.

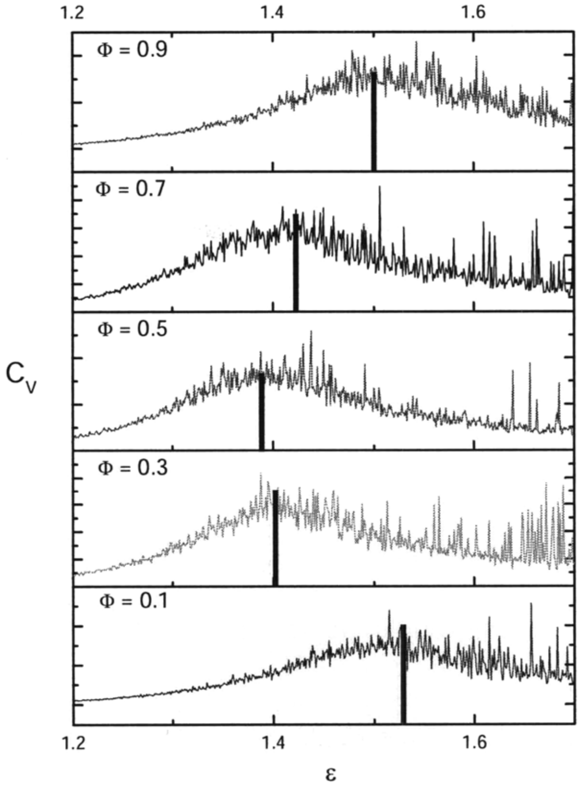

Figure 3: A comparison of specific heat peaks for different volume fractions. Note that values are omitted on the y-axis because the values are only an approximation to C_V and have no meaning; only the value of ε for which a peak is obtained has significance (bar drawn to show peak value).

Figure 4 shows the phase diagram derived from the data in Figure 3. To illustrate the difference in the phase separated versus mixed region, images of the nanoparticle in each of the regions is shown. Visual confirmation of phase separation confirms the accuracy of the phase diagram.

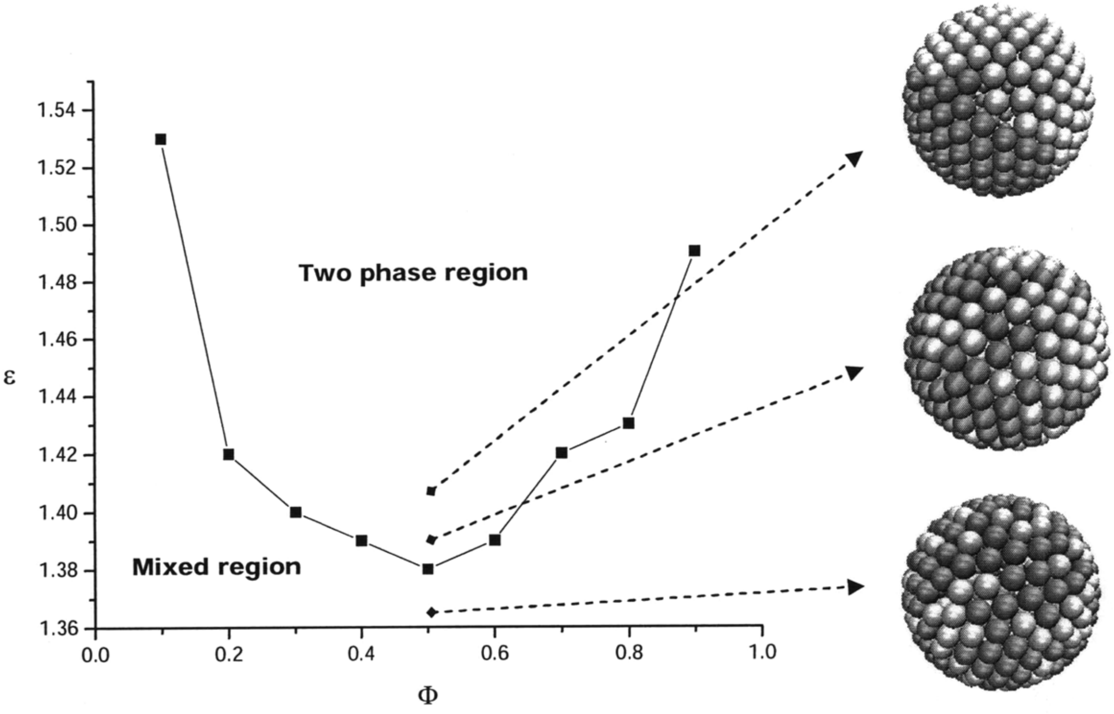

Figure 4: Phase diagram of nanoparticle surface, with images drawn to illustrate phase behavior.

The phase diagram results illustrate the efficacy of the Ising-inspired model for analyzing phase behavior of the nanoparticle surface. While a striped phase does not appear spontaneously under this model, the formation of stripes would imply a preference for neither strong phase separation nor mixing. Hence, it is expected that choosing values of ε near the phase transition would best model the surface behavior of striated nanoparticles.

B. "Ghost membrane"

The "ghost membrane" simulations were performed for a range of ε values and for two ε_B values, illustrating the influence of weak and strong bilayer interactions. Results for simulations run with surface mobility enabled are shown in Figure 5. For comparison, an energy diagram of a particle with rigid striped phases with energy calculated using $\varepsilon = 1.4$ and $\varepsilon_B = 5.0$ is shown in Figure 6.

The shape of the energy diagram for the nanoparticle coated in rigid stripes implies that passage is unlikely under the current model. A spike in total energy is associated with each successive stripe crossing the boundary between different head and tail regions of the bilayer, and the large number of such spikes would impose a significant barrier to entry. By comparison, when ligand mobility is enabled the overall trend in total system energy as the nanoparticle passes through the membrane is negative, implying that the nanoparticle will preferentially travel to the middle of the bilayer. As the strength of interaction with the bilayer increased, however, several discontinuities appear in the energy diagram only as the particle enters. The discontinuity occurs for the same z-value independent of the nanoparticle's order parameter, implying a geometric constraint. This hypothesis is confirmed by visual examination as illustrated in Figure 7; as the nanoparticle progresses into the bilayer, hydrophilic beads preferentially align in the head region, creating a layer of white beads as shown in image 2. As the particle continues to progress, more and more hydrophilic beads attempt to align with the head region, resulting in hydrophilic beads being pushed into the unfavorable tail region. The

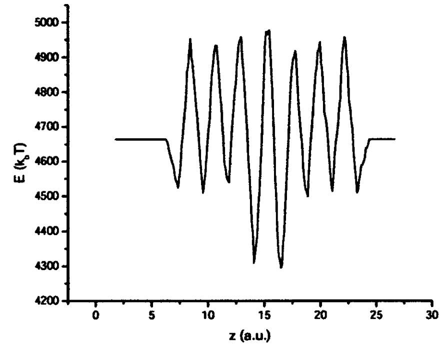

Figure 5: Nanoparticle energy for particle with rigid, striped liands passing through the ghost membrane. The large fluctuations in energy with the passage of each successive stripe provide a barrier to particle passage

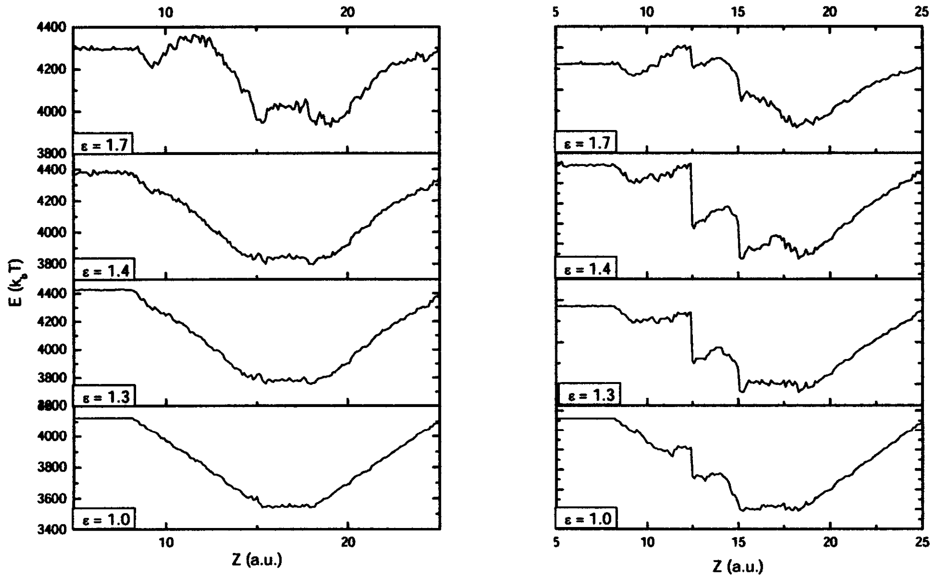

Figure 6: Plots of nanoparticle energy as a function of z-axis distance. Interaction with the bilayer begins at z = 7, and continues to z = 25. The series of four plots illustrates the energy landscape for values of ε far from the phase transition (ε = 1.0, 1.7) and near the phase transition (ε = 1.3, 1.4). The left series of plots is for weak bilayer interaction ($\varepsilon_B = 3.0$) while the right series of plots is for stronger bilayer interaction ($\varepsilon_B = 5.0$). Note that no units are specified as the energy parameters have no physical analogue.

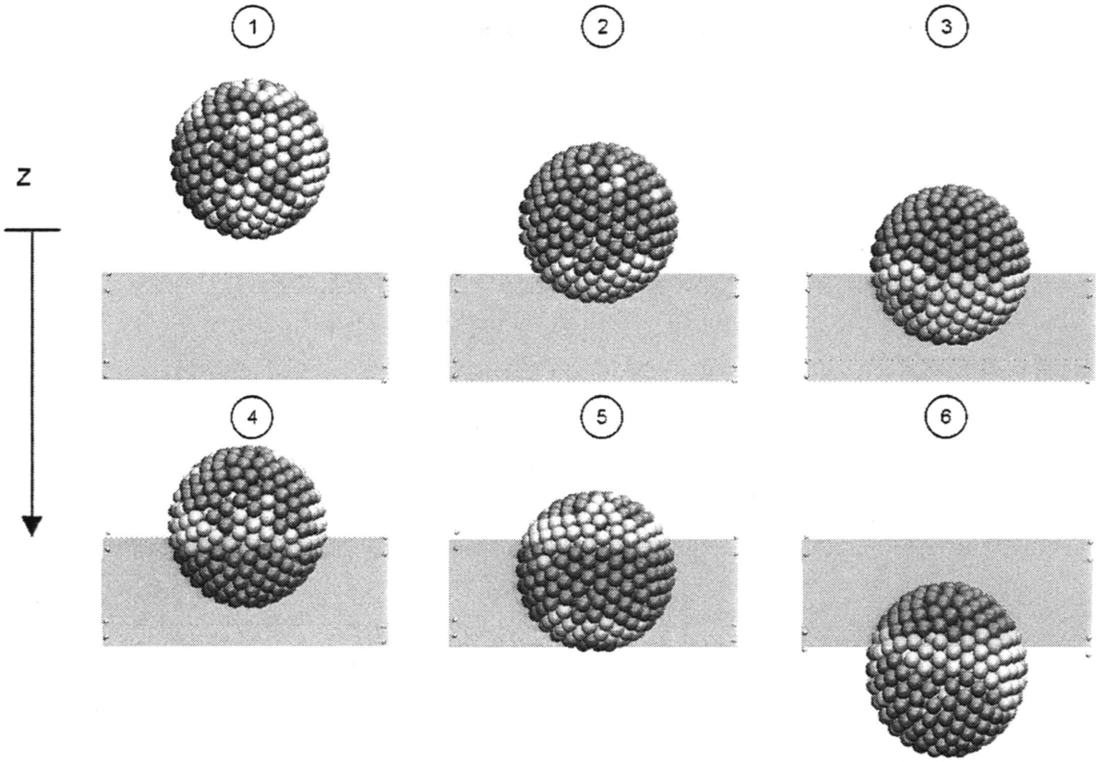

Figure 7: Images of nanoparticle interaction with "ghost bilayer" at $\varepsilon = 1.4$, $\varepsilon_B = 5.0$; for corresponding energies, see Figure 6. Red bars indiciate bilayer head regions, while blue bars indicate bilayer tail regions, with grey beads acting as markers for region boundaries.. Image 1 shows nanoparticle near phase transition point prior to entry to bilayer. Image 2 shows initial contact with bilayer, with hydrophilic beads preferentially moving to interact, inducing phase separation. Image 3 occurs just before the discontinuity seen in Figure 3. Image 4 occurs immediately after the discontinuity; hydrophobic beads have now reorganized into the tail region of the bilayer. Image 5 shows the nanoparticle divided into 5 different phases. Finally, image 6 illustrates the symmetry with image 4 as the nanoparticle leaves the bialyer; no discontinuity occurs upon exit.

hydrophilic beads act as a barrier preventing hydrophobic beads from migrating into the more energetically favorable tail region until the discontinuity is reached; once the particle progresses to a certain distance, hydrophobic beads are finally forced into the head region, resulting in an unfavorable interaction. A minimum is then established when the hydrophobic beads migrate into the tail region, permitting hydrophilic beads to again realign with the head region as illustrated in image 4. A similar effect leads to another discontinuity resolving to an ordering as shown in image 5; in general, the large drops in energy can be associated with the nucleation of a new, ordered phase on the surface of the nanoparticle.

The discontinuity behavior gives insight into some of the observed experimental behavior. For high values of the nanoparticle order parameter ε, there is a significant energy barrier prior to the large energy drop due to the discontinuity, while for values of ε near and below the phase transition this barrier disappears, greatly increasing the likelihood of nanoparticle entry. The presence of this barrier for high values of ε, corresponding to highly phase-separated particles, could explain the inability of these particles to penetrate the bilayer. Note that the discontinuity is also a feature of initial penetration only, and does not appear when the nanoparticle leaves the membrane, regardless of whether the particle continues to progress in the same or opposite direction.

One issue with examining the energy landscape alone is it does not explain the inability of nanoparticles with randomly ordered ligands, the low ε case, to penetrate the nanoparticle. It is important to note that the graphs as drawn above are of average energy of the system, and do not include a contribution due to entropy; what is of most interest in this system is the free energy landscape, as minimization of free energy will ultimately determine whether or not particles can easily penetrate the membrane. Given the ordering imposed by the bilayer interaction, a corresponding decrease in entropy would be expected, leading to a different free energy profile.

The entropic contribution to free energy should also be dependent on ε. Figure 8 illustrates the separation of the total energy profile into contributions from bilayer interactions and particle surface interactions for ε = 0.5. The interaction with the bilayer forces beads on the nanoparticle to sample energetically unfavorable configurations since mixing is favored; hence, there may be a strong entropic cost resulting in an undesirable free energy landscape. To fully understand the ghost membrane, then, it is necessary to fully compute the free energy landscape versus just the internal energy of the system.

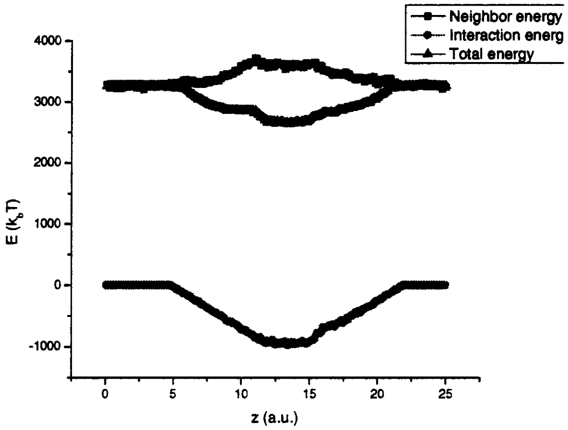

Figure 8: Contribution to total energy landscape from both neighbor interactions and bilayer interactions for ε = 0.5. While bilayer interactions are dominant and lead to a negative total energy change, forced phase separation on the surface leads to a positive contribution from the neighbor energy term.

IV. CONCLUSION

The formulation of a "ghost membrane" technique for analyzing the interaction between a nanoparticle with mobile ligands and a disrupted bilayer illustrated the relation between nanoparticle position with respect to the bilayer and system energy. Initial results support the hypothesis that in this ideal case, the energy of the system would in fact be lowered by the penetration of the nanoparticle into the bilayer. A discontinuity related to geometric factors was identified which provides an energy barrier to entry, explaining the inability of phase-separated particles to penetrate. However, this approach did not actually identify the free energy of the particle-bilayer interaction, and thus neglects the effect of entropic considerations on the mechanism. The additional influence of entropic effects may explain why particles with mixed bead concentrations are unable to penetrate the bilayer, and hence the next step in research will be calculating the free energy of the system.

CHAPTER 3: Brownian Dynamics Simulation

I. INTRODUCTION

The primary means of determining the mechanism of membrane penetration was via a coarse-grained Brownian Dynamics model of bilayer and nanoparticle interaction. A solvent-free model of a lipid bilayer with behavior mimicking physical systems was simulated with minimal computational cost. A nanoparticle was then constructed at a similar length scale and used to model the interaction between the bilayer and particle.

The Monte Carlo simulation governing the behavior of the nanoparticle surface as described in Chapter 2 was also utilized in this simulation. By enabling or disabling the MC simulation, the nanoparticle could be made to mimic static nanoparticles with ordered domains as described in the original work or could be made to show surface fluctuations. It is proposed that the mechanism for entry depends primarily upon the surface fluctuations modeled by the MC simulation, and that particles lacking adequate surface mobility will fail to penetrate the bilayer.

II. METHODS

A. Bilayer Simulation

For the coarse-grained lipid bilayer model, a Brownian Dynamics scheme was implemented, utilizing a previously developed[15] 3-bead solventless model to simulate the bilayer. This model has been successfully used to study simple cellular endocytosis[16] and membrane interactions with viral capsids[17]. The solventless methodology was employed to minimize computation time; in place of explicit solvent molecules, long-range attractive interactions were employed to give the bilayer structural properties.

Each lipid in the bilayer was composed of three distinct beads, one representing a hydrophilic head and two representing the hydrophobic tail. The structure of the bilayer was created via the application of four potentials. These potentials are defined as follows, and are illustrated in Figure 9:

1) A Weeks-Chandler-Anderson (WCA) repulsive potential between all beads, enforcing a hard-sphere model:

$$V_{WCA}(r) = \begin{cases} 4\varepsilon\left[(b/r)^{12} - (b/r)^{6} + \frac{1}{4}\right], & r \leq r_c \\ 0, & r > r_c \end{cases}$$

2) An harmonic potential between consecutive beads in a single lipid, enforcing lipid stability:

$$V_{harm}(r) = \frac{1}{2} k_{harm} (r - \sigma)^2$$

3) An harmonic potential between the head bead and second tail bead in a lipid, ensuring limited rigidity:

$$V_{bend}(r) = \frac{1}{2} k_{bend} (r - 4\sigma)^2$$

4) An attractive force between all tail beads in different lipids, providing the primary tunable force to determine bilayer phase (a graph of the force is shown in Figure 9):

$$V_{attr}(r) = \begin{cases} -\varepsilon, & r < r_c \\ -\varepsilon \cos^2\left[\pi(r - r_c)/2w_c\right], & r_c \leq r \leq r_c + w_c \\ 0, & r > r_c + w_c \end{cases}$$

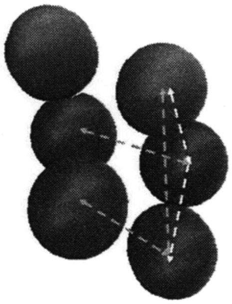

Figure 9: Illustration of forces acting on bilayer beads, independent of nanoparticle interaction. White lines represent FENE bonds between beads comprising the same lipid. Orange lines represent attractive forces between tail beads of different lipids. The green line represents the bending force between the head and second lipid beads. While not shown, the WCA force prevents beads from overlapping.

Two additional potentials were imposed to account for nanoparticle/bilayer interaction at the coarse-grained level. These were:

1) A Lennard-Jones (LJ) potential accounting for electrostatic interactions between head beads in the bilayer and hydrophilic beads on the nanoparticles:

$$V_{LJ}(r) = \begin{cases} 0, & r \le r_c \\ 4\varepsilon\left[(b/r)^{12} - (b/r)^{6}\right] & r > r_c \end{cases}$$

2) An exponential repulsive potential between tail beads in the bilayer and hydrophilic beads on the nanoparticle, accounting for hydrophobic effects:

$$V_{rep}(r) = 2r_c e^{-r/2R_c}$$

Figure 10 shows the comparison in strength between the respective potentials and forces.

B. Nanoparticle assembly

Nanoparticle assembly was accomplished by imposing three forces upon particle beads: a WCA force as with the bilayer beads, fixing bead volume; a spring force between each bead on the surface of the particle to a bead in the center, fixing the particle radius and spherical shape; and finally spring forces to each bead's nearest neighbors, providing further rigidity on the particle surface. The beads all were placed at the center and then allowed to move randomly away from the center before the sphere was assembled by imposition of the aforementioned forces. A single bead was still retained in the center – manipulation of the full nanoparticle was thus accomplished by simply applying forces to

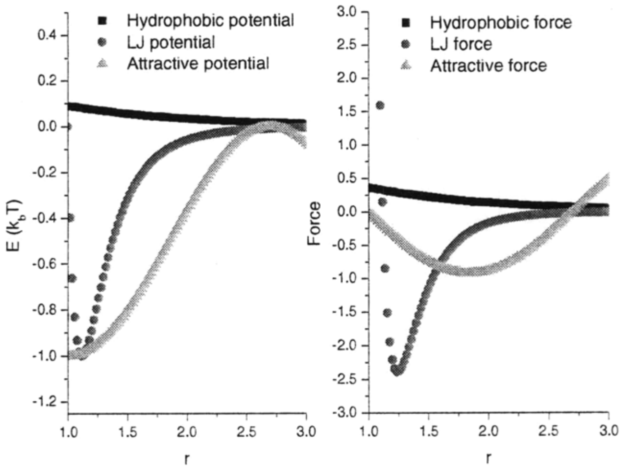

Figure 10: Comparison between membrane-nanoparticle interaction forces and potentials, compared to the attractive force responsible for membrane structure.

the center bead. Finally, bead types (hydrophobic or hydrophilic) could be assigned either randomly or by explicitly creating stripes.

C. Algorithm

A Brownian Dynamics (BD) algorithm was used to model the bilayer and interaction with nanoparticles[18]. While Appendix A gives a more detailed derivation of BD, the basic algorithm is to numerically solve the following equation for each bead:

$$\tilde{r}(t+\Delta t) = \tilde{r}(t) + \Delta\tilde{t}\,\tilde{F}_{n-h} + \sqrt{2\Delta\tilde{t}}\,\tilde{\xi}$$

where $\tilde{r}(t)$ is a given bead's position at time t, $\Delta\tilde{t}$ is the dimensionless stepsize, $\tilde{F}_{n-h}$ is the net non-hydrodynamic force on a given bead calculated from the potentials defined above, and ξ is a stochastic operator, given by a Gaussian distribution with variance of one. The inclusion of the stochastic operator adds random fluctuations to account for the influence of temperature in the simulation.

An identical Monte Carlo algorithm as that defined in Chapter 2 was utilized to control the movement of beads on the surface of the nanoparticle. Bilayer interaction was still controlled by an energy parameter ε_B, but given that membrane curvature did not permit for easily defined interaction regions, interaction was instead defined by energetic contributions from the bilayer. The potential of each position on the surface of the nanoparticles was calculated, allowing the change in energy for a potential swap to be determined. If the change in energy was negative, a factor of $-2\varepsilon_B$ was applied to the energy of the swap, analogous to the change in energy when moving a bead to a more energetically favorable position in the ghost membrane simulation. If the initial bead position had an energy of zero, then a factor of only $-\varepsilon_B$ was applied, equivalent to moving a bead from a position outside of the bilayer to a region of interaction. Positive energies were added if the switch would lead to an increase in potential. Hence, the Monte Carlo algorithm used in the BD simulation was similar to that of the ghost membrane.

D. Verlet list optimization

A simple implementation of a Verlet algorithm was utilized to optimize the BD process[19]. By this method, each bead stored a list of near-neighbor beads defined within a certain cutoff radius. At each timestep, interactions were calculated between each bead and its neighbors only, while ignoring interactions between non-neighboring beads. The near-neighbor lists were updated every fixed number of timesteps to ensure accuracy. While the process of updating the near-neighbor lists ran in O(n^2) time, calculating forces occured in O(n) time. By ensuring that lists were updated infrequently, runtime efficiency was greatly improved when compared to the expense of calculating all possible force pairs each timestep (even if ignoring interactions via a cutoff radius).

In order to optimize the Verlet algorithm, it was necessary to find both the combination of cutoff radius and number of timesteps between near-neighbor list updates that allows for fastest runtime. For any given cutoff radius, the number of timesteps between near-neighbor updates was equivalent to the *correlation time* for that radius, defined by the amount of time between correlated events in the simulation. The correlation time for a particular Verlet radius was calculated by tracking a *correlation matrix*, defined as a two-dimensional matrix such that each element

$$[i(t), j(t)] = \begin{cases} 1, & r < r_{cutoff} \\ 0, & r \geq r_{cutoff} \end{cases}$$

where r is the distance between beads i and j at time t and r_{cutoff} is the Verlet radius.

With this representation, each row of the matrix gave the near-neighbors for the ith bead, and the sum of all elements in the matrix divided by the total number of beads was the average number of near-neighbors per bead at a given timestep. The matrix was updated every timestep with the condition that once an element was 0, it could not revert to 1; hence, the average number of neighbors per bead necessarily decreased with time. The *correlation time* was then defined as the number of timesteps necessary for the average number of neighbors to decrease to $1/e$ the initial value. Larger values of the Verlet radius would have longer corresponding correlation times, as the initial number of near-neighbors would be higher and the time taken for the average value to decrease would take longer. Tuning the algorithm to find the optimal combination of Verlet radius and correlation time thus relied on two competing factors – increasing the value of the

Verlet radius would cause each bead's near-neighbor list to be greater, requiring more iterations per timestep at O(n) time, but would have a longer correlation time, requiring fewer updates of $O(n^2)$ time.

To find the optimal Verlet radius, a range of Verlet radii between the values of 3σ and 5σ were tested in increments of 0.01σ. The minimum value of 3σ was chosen to ensure that enough neighbors were included to generate an accurate simulation. With each value, the correlation time was first determined via the correlation matrix above, then the simulation was rerun using the calculated correlation time for a 200,000 timestep simulation of a 600 bead bilayer with values of $w_c = 1.6$ and $\varepsilon = 1.0$. Figure 11 shows that runtime consistently decreased as correlation time increased, implying that the minimum possible correlation time was desirable. For a minimum Verlet radius of 3σ this resulted in a correlation time of 25,000 timesteps.

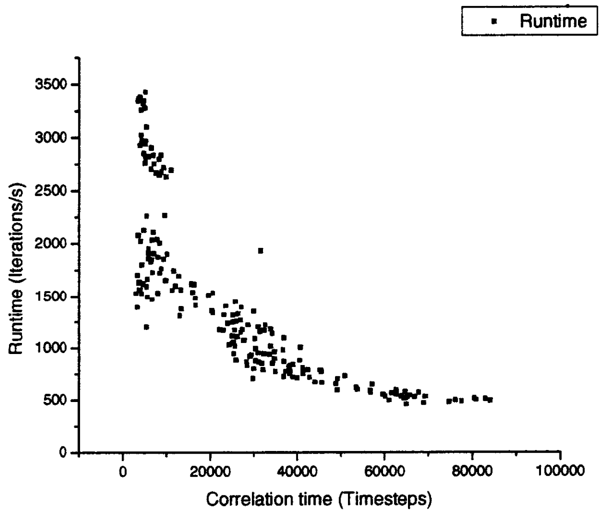

Figure 11: Runtime as a function of correlation time, which additionally scales with verlet radius. Given that runtime consistently decreases, the optimal correlation time was chosen based on a desired verlet radius of 3.0 to ensure that all force interactions were adequately captured. This yielded a correlation time of about 25,000 timesteps.

E. Bilayer characterization

To ensure that the simulation accurately modeled bilayers, two primary tuning parameters were varied: w_c, the range of the attractive potential, and ε, the unit of energy used to define the strength of the WCA and attractive forces and equivalent to a leading coefficient on $k_b T$. These two parameters controlled the formation of three distinct bilayer phases: a gel phase with minimal membrane fluctuations and solid-like properties, a fluid phase, and a gas phase representing complete break up of the bilayer (which has no analog in physical systems). Varying the two tuning parameters allowed a phase diagram to be developed.

III. RESULTS AND DISCUSSION

A. Bilayer phase diagram

Phase characterization was accomplished by visual inspection and calculation of the bilayer diffusion constant. To calculate the diffusion constant, the distance each head bead travelled was first tracked for the length of a simulation. The diffusion coefficient was then calculated via the formula

$$D(\Delta t) = \frac{1}{N}\sum_{n=0}^{N}\frac{x_n(\Delta t)^2}{6\Delta t}$$

where Δt is the number of timesteps between measurements and $x_n(\Delta t)$ was the distance travelled by bead *n* in the given time period, and *N* is the total number of beads in the simulation. Figure 12 shows the results of diffusion constant calculations for a few characteristic examples; as expected, the gel phase had the lowest value of *D*, while the gas phase had the highest by large margin.

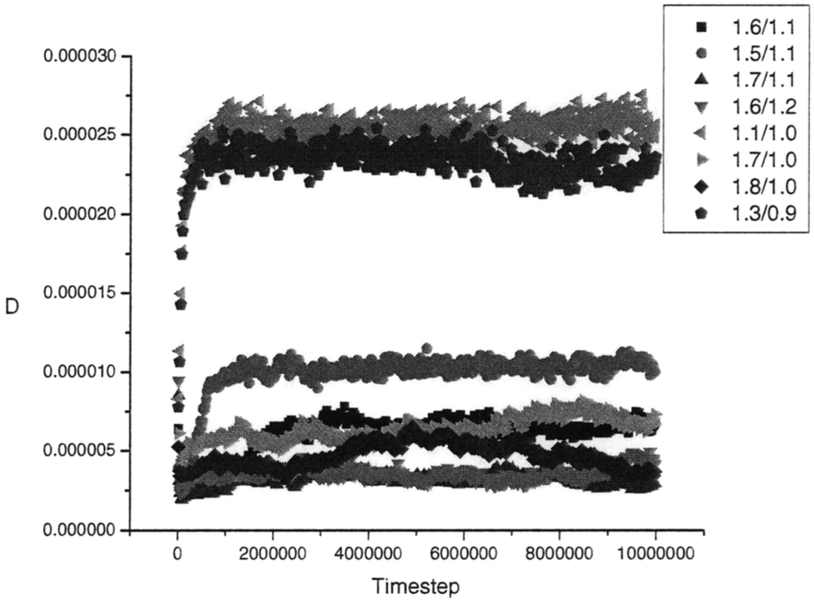

Figure 12: Diffusion constants as a function of time for a variety of system parameters. Increasing either parameter tended to decrease the diffusion constant.

Visually, each phase showed characteristic qualities as illustrated in Figure 13. The gas phase was easily recognizable via the onset of complete systemic disorder. The fluid phase was characterized by long range order coupled with undulations along both the x- and y-axis, as well as occasional pore formation matching physical expectations[20]. The gel phase appeared similar to the fluid phase, but was generally more planar; some gel phases additionally formed unique "stacked" conformations as illustrated in Figure 14. The combination of visual characteristics and diffusion constant data allowed for the generation of the phase diagram as shown in Figure 15. Based on this data, the choices of parameters that gave the most accurate physical behavior were w_c = 1.7 and ε = 1.0. These parameters were used in the remainder of the experiments.

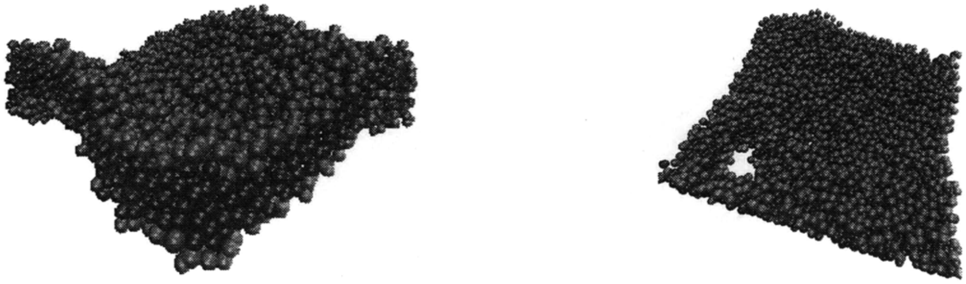

Figure 13: Illustration of characteristic fluid behavior in 30x30 lipid simulation with $w_c = 1.7$ and $\varepsilon = 1.0$.The image on the left shows undulations in both x- and y-axes of the bilayer, while the image on the right shows pore formation.

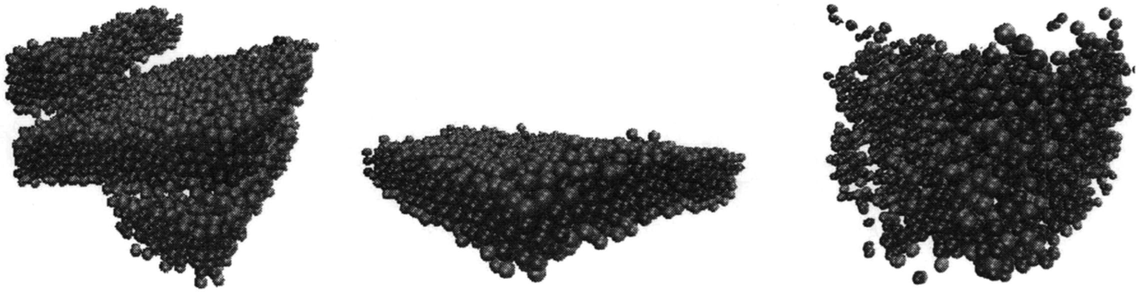

Figure 14: Illustration of characteristic gel behavior (left 2 images) and gas behavior (right image) in 30x30 lipid simulation with $w_c = 1.7$ and $\varepsilon = 1.1$, $w_c = 1.8$ and $\varepsilon = 1.0$, and $w_c = 1.3$ and $\varepsilon = 0.8$ respectively. The leftmost image depicts a stacked gel phase that formed spontaneously. The middle image displays the lack of undulation and generally planar geometry consistent with gels. The right most image shows the breakup of the bilayer into a gas.

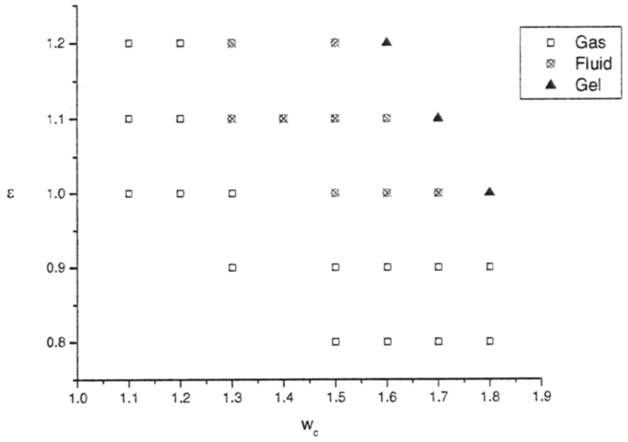

Figure 15: Bilayer phase diagram, showing the formation of distinct gel, fluid, and gas phases. The optimal values for physical simulations were $w_c = 1.7$ and $\varepsilon = 1.0$ based on bilayer characterization techniques; as expected, the gel phase was preferred for larger values of $w_c = 1.7$ and ε.

B. Nanoparticle penetration

The simulation did show that the nanoparticle was capable of penetrating the bilayer with a surface concentration $\Phi = 0.5$ and with nanoparticle parameters $\varepsilon = 1.4$ and $\varepsilon_B = 5.0$. A force of 10 k_bT/nm was applied to slightly push the nanoparticle into the membrane. We observed induced poration as mechanism of entry, as shown in Figure 16. As the nanoparticle approached the bilayer, beads on the surface reorganized to bring hydrophilic beads in contact with the head beads of the bilayer. As the membrane undulated, phase separation occurred on the surface of the particle, further encouraging the membrane to wrap around the particle. This wrapping promoted pore formation as the increased curvature of the membrane applied tension to the lower surface of the bilayer, leading to disruption. Note that as shown in image 3, the hydrophobic beads would preferentially realign with the pore as it formed as hydrophilic beads occupied positions on the nanoparticle more favorable for interaction with the bilayer heads. The continued downward motion of the particle as a result of the applied force led to the formation of a larger pore, until eventually the nanoparticle passed completely through. Note that during this entire process, the bilayer maintained stability until the pore eventually reformed, as is partially shown in image 6.

Penetration by poration is consistent with the behavior observed by cationic nanoparticles[10], which is mimicked by the realignment of hydrophilic beads to preferred positions near the interface of the nanoparticle and bilayer. Similar penetration behavior is observed in models of peptides as well[21]. Repeating the simulation with a particle coated entirely in hydrophilic beads confirmed that a cationic particle would successfully induce pore formation and penetrate by the same mechanism.

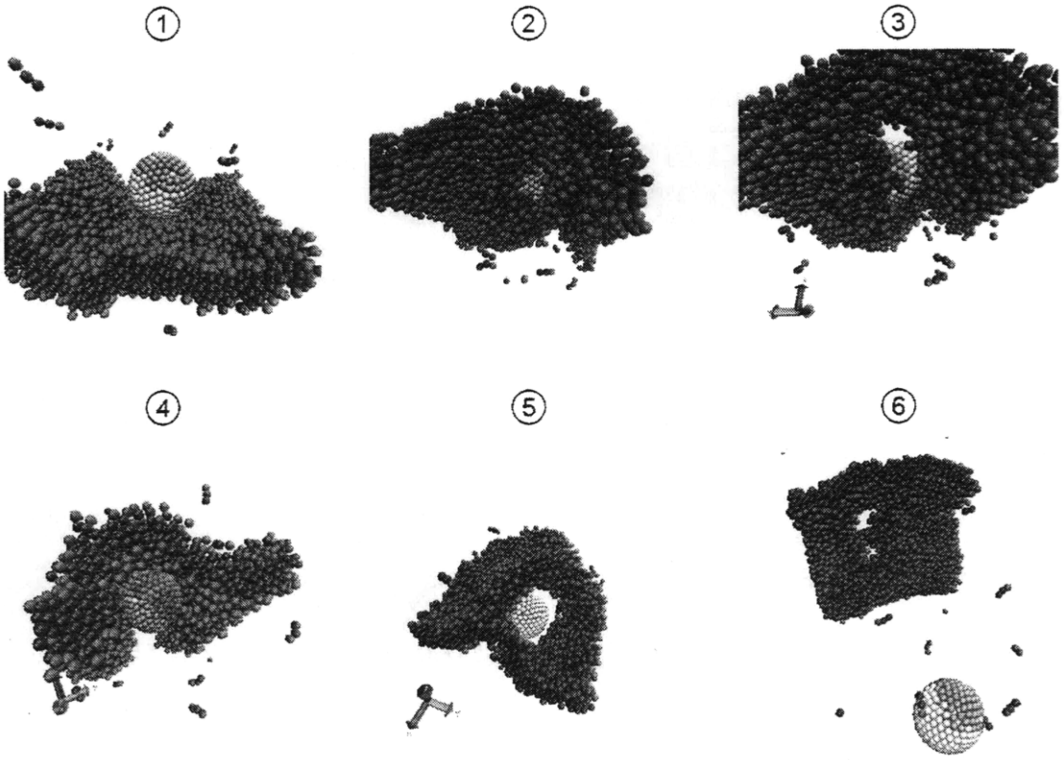

Figure 16: Images of bilayer penetration by nanoparticle with Φ = 0.5, ε =1.4 and ε_B = 5.0, and with constant applied force of 5 $k_b T$. Image 1 shows initial contact and realignment of hydrophilic beads near bilayer heads. Image 2 shows onset of membrane wrapping .Image 3 shows pore opening, with alignment of hydrophobic beads. Image 4 shows continual pore expansion. Image 5 shows passage of particle through bilayer. Image 6 illustrates undisrupted structure of bilayer after nanoparticle has passed through.

Hence, it seems that surface mobility for this set of parameters causes the nanoparticle to mimic a fully cationic particle.

A simulation run with a particle set in the striped conformation but without surface mobility was unable to penetrate the membrane, even with the same force applied. Figure 17 shows the nanoparticle rotating along the surface of the bilayer to align with as many hydrophilic beads on the surface as possible.

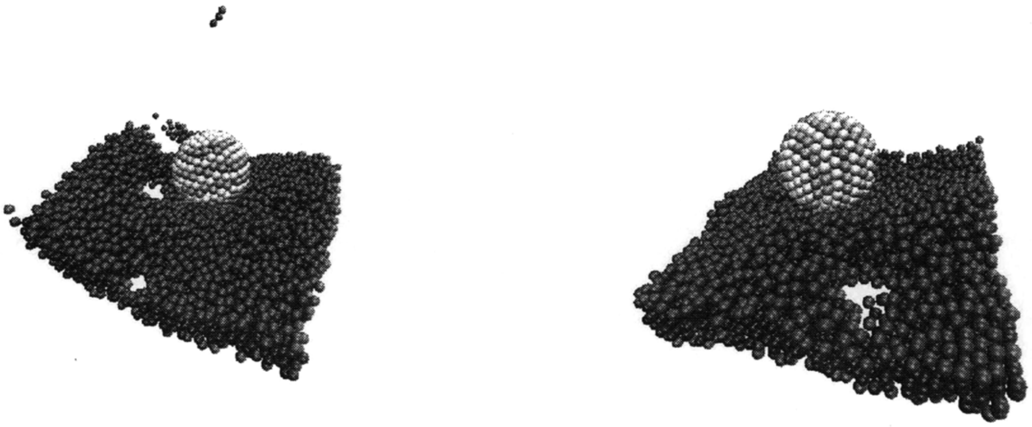

Figure 17: Striped nanoparticles without the benefit of surface mobility are unable to penetrate the bilayer.

Simulation results were also highly dependent on system parameters. Modifying the strength of the Lennard-Jones potential, for example, led to vesicle formation rather than membrane penetration for a particle coated in hydrophilic beads, a result in agreement with Reynwar[17]. Figure 18 illustrates membrane wrapping prior to vesicle formation. This result corresponds well with the experimental observation of non-striped beads existing largely in endosomal compartments. Further modification of system parameters thus might lead to disruptive interactions between the nanoparticle and bilayer that correlate to the proposed reaction mechanism.

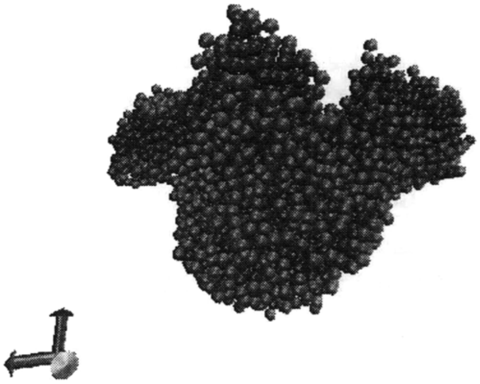

Figure 18: Wrapping of nanoparticles when Lennard-Jones interaction is increased.

V. CONCLUSIONS

A functional, physically accurate lipid bilayer model was adapted to model the interaction of cellular membranes with nanoparticles coated in different amounts of hydrophilic and hydrophobic ligands. Based on a 3-bead solventless Brownian Dynamics simulation, three distinct bilayer phases were identified that corresponded well with real systems.

Initial simulations have shown penetration by poration as the likely reaction mechanism. While experimentally poration was ruled out due to no detectable leakage of cytosol, the small diameter of pores formed in this simulation implies that no cytosol leakage would be observed, consistent with experiments. No permanent bilayer disruption was observed in the course of the simulation for the parameters chosen. However, disruptive behavior was observed when simulation parameters, such as the strength of the attractive Lennard-Jones potential, were changed. Hence, future work will consist of further refinement of parameters governing both the interactions between the bilayer and nanoparticle (e.g. the Lennard-Jones potential, and repulsive hydrophobic potential) and the surface properties of the nanoparticle (e.g. phase separation properties).

CHAPTER 4: Conclusions and Future Work

A. Conclusions

Using an Ising-inspired model to calculate system energy, we implemented a Monte Carlo simulation to model the movement of mobile ligands on the surface of a nanoparticle. This model enabled us to derive a phase diagram for the separation behavior between "hydrophobic" and "hydrophilic" beads on the nanoparticles surface, based on a single order parameter ε. By modeling the bilayer as a static field, the average energy of interaction between the nanoparticle and bilayer was calculated as a function of ε , confirming that values of ε promoting mixing rather than phase separation led to favorable bilayer-nanoparticle interactions.

A coarse-grained Brownian Dynamics simulation was developed to model the reaction mechanism of bilayer penetration. A 3-bead solventless lipid bilayer model with broad attractive interactions developed by Cooke and Deserno was used. By varying two system parameters, a bilayer phase diagram with three distinct phases was developed, in agreement with both experimental and theoretical results. Introduction of a nanoparticle, with surface mobility governed by the same Monte Carlo simulation as before, allowed for exploration of the reaction mechanism. The simulation demonstrated that striped nanoparticles without surface mobility could not penetrate the membrane, even when a small force was applied. Nanoparticles with surface mobile ligands were able to penetrate by inducing the formation of small pores which enabled particle passage before reforming. These pores were small enough to not permit the loss of cytosol from the cell, agreeing with experimental results.

B. Future work

As the "ghost membrane" simulation only calculated the average total energy of the bilayer-nanoparticle system, it did not adequately explore the entropic contributions to free energy which might alter the likelihood of bilayer penetration. Future work in this simulation will focus on developing a full free energy dependence on ε, which may illustrate why very low ε cases do not penetrate the bilayer.

Future work on the coarse grained model will continue to explore the reaction mechanism observed. Varying system parameters such as the strength of the Lennard-Jones potential will hopefully illustrate what conditions are necessary for penetration to occur. Similarly, penetration will be tested using different values of ε, different particle sizes, and different ratios of hydrophobic to hydrophilic beads in order to identify what tuning parameters are most important in membrane penetration. Changing the number of Monte Carlo timesteps per Brownian Dynamics timestep will also illustrate the effect of the rate of surface reconstruction on the nanoparticles. Finally, it will be interesting to see the effect of external conditions that might occur *in vivo*, such as the addition of a shear force to the system due to blood flow.

References

---

[1] Pridgen, E.M; Langer, R.; and Far okhzad, O.C. Biodegradable, polymeric nanoparticles delivery systems for cancer therapy. *Nanomedicine* **2**, 669-680 (2007).

[2] Kukowska-Latallo, J. F.; Candido, K. A.; Cao, Z. Y.; Nigavekar, S. S.; Majoros, I. J.; Thomas, T. P.; Balogh, L. P.; Khan, M. K.; Baker, J. R. Nanoparticle targeting of anticancer drug improves therapeutic response in animal model of human epithelial cancer. *Cancer Res.* **2005**, *65*, 5317–5324.

[3] Jackson, A. M., Myerson, J. W. & Stellacci, F. Spontaneous assembly of subnanometre-ordered domains in the ligand shell of monolayer-protected nanoparticles. *Nature Mater.* **3**, 330–336 (2004).

[4] Verma, A. *et al.* Surface-structure-regulated cell-membrane penetration by monolayer-protected nanoparticles. *Nature Materials* **7**, 588-595 (2008).

[5] Allen, T. M. & Cullis, P. R. Drug delivery systems: Entering the mainstream. *Science* **303**, 1818–1822 (2004).

[6] Stewart, M. Molecular mechanism of the nuclear protein import cycle. *Nat. Reviews Mol. Cell Bio* **8**, 195-208 (2007).

[7] Han, G.; Ghosh, P.; Rotello, V. Functionalized gold nanoparticles for drug delivery. *Nanomedicine* **2**, 113-123 (2007).

[8] Takeuchi, T. *et al.* Direct and rapid cytosolic delivery using cell-penetrating peptides mediated by pyrenebutyrate. *ACS Chem. Biol.* **1**, 299–303 (2006).

[9] Kopatz, I.; Remy, J. S.; Behr, J. P. A model for non-viral gene delivery: through syndecan adhesion molecules and powered by actin. *J. Gene Med.* 2004, **6**, 769–776.

[10] Leroueil, P. R. *et al.* Nanoparticle interaction with biological membranes: Does nanotechnology present a janus face? *Acc. Chem. Res.* **40**, 335–342 (2007).

[11] Lovric, J. *et al.* Differences in subcellular distribution and toxicity of green and red emitting CdTe quantum dots. *J. Mol. Med.* **83**, 377–385 (2005).

[12] Singh, C, *et al.* Entropy-Mediated Patterning of Surfactant-Coated Nanoparticles and Surfaces. *Physical Review Letters* **99**, 226106 (2007).

[13] Kratzer, P. Monte Carlo and kinetic Monte Carlo methods. *Condensed Matter – Materials Science* [SUBMITTED FOR REVIEW].

---

[14] Allen, MP. and Tildesley, DJ. Computer Simulation of liquids. Oxford University Press, New York (1992).

[15]Cooke, I. R and Deserno, M. Solvent-free model for self-assembling fluid bilayer membranes: Stabilization of the fluid phase based on broad attractive tail potentials. *J. of Chem. Phys* **123**, 224710 (2005).

[16] Cooke, IR, and Deserno, M. Coupling between lipid shape and membrane curvature. *Biophysical Journal* **19,** 487-495 (2006).

[17] Reynwar, B. *et al.* Aggregation and vesiculation of membrane proteins by curvature-mediated interactions. *Nature* **447**, 461-464 (2007).

[18] Ermak, D.L. and McCammon, J.A. Brownian dynamics with hydrodynamic interations. *J. of Chem. Phys* **69**, 1352-1360 (1978).

[19] Chialvo, A.A. and Debenedetti, P.G. On the use of the verlet neighbor list in molecular-dynamics. *Computer Physics Communications* **60**, 215-224 (1990).

[20] Dimitrov, D.S. and Jain, R. K. Membrane stability. *Biochem. Biophys. Acta* **779**, 437-468 (1984).

[21] Illya, G. and Deserno, M. Coarse-grained simulation studies of peptide-induced pore formation. *Biophysical Journal* **95**, 4163-4173 (2008).

APPENDIX: Brownian Dynamics

The derivation of Brownian Dynamics assumes a system of particles interacting with some solvent, with the further assumption that the net force on any given particle is ≈ 0. From Newtonian mechanics, this gives:

$$F_{net} = F_{drag} + F_{non-hydrodynamic} + F_{Brownian} = 0$$

where F_{drag} is the drag force on the particle from the solvent, $F_{non-hydrodynamc}$ is the sum of forces between beads, and $F_{Brownian}$ is a random force accounting for Brownian motion.

Assuming slow speeds and low turbulence, $F_{drag} = -b\frac{d\vec{r}}{dt}$ by Stoke's theorem where b is the drag coefficient. Substituting and rearranging yields:

$$\frac{d\vec{r}}{dt} = \frac{1}{b}\left(F_{non-hydrodynamc} + F_{Brownian}\right)$$

To simplify this equation, let $\mu = \frac{1}{b}$ and $\vec{\xi} = \frac{1}{b}F_{Brownian}$, yielding the governing equation of BD:

$$\frac{d\vec{r}}{dt} = \mu F_{n-h} + \vec{\xi}$$

The goal of BD is to solve this differential equation numerically. Approximating for small time differences Δt yields:

$$\vec{r}(t + \Delta t) = \vec{r}(t) + \Delta t\left(\mu F_{n-h} + \vec{\xi}\right)$$

Next, make position dimensionless by dividing by bead radius r_c and make all forces dimensionless by multiplying by $\frac{r_c}{k_b T}$. Denoting dimensionless variables with ~ gives:

$$\tilde{r}(t+\Delta t)=\tilde{r}(t)+\frac{\Delta t}{r_c}\left(\frac{r_c}{k_bT}\right)\frac{\mu F_{n-h}}{r_c/k_bT}+\frac{\Delta t}{r_c}\vec{\xi}$$

$$\tilde{r}(t+\Delta t)=\tilde{r}(t)+\frac{\Delta t}{r_c}\left(\frac{\mu k_bT}{r_c}\right)\frac{r_cF_{n-h}}{k_bT}+\frac{\Delta t}{r_c}\vec{\xi}$$

$$\tilde{r}(t+\Delta t)=\tilde{r}(t)+\frac{\mu k_bT\Delta t}{r_c^{\,2}}\tilde{F}_{n-h}+\frac{\Delta t}{r_c}\vec{\xi}$$

Using the Einstein relation $D=\mu k_bT$, with $\mu=\frac{1}{b}$ in this low Reynolds number limit, and recognizing that $\langle r_c^{\,2}\rangle=6D\tau=6\mu k_bT\tau\rightarrow\frac{1}{6\tau}=\frac{\mu k_bT}{r_c^{\,2}}$, yields:

$$\tilde{r}(t+\Delta t)=\tilde{r}(t)+\frac{\Delta t}{\tau}\tilde{F}_{n-h}+\frac{\Delta t}{r_c}\vec{\xi}$$

$$\tilde{r}(t+\Delta t)=\tilde{r}(t)+\Delta\tilde{t}\tilde{F}_{n-h}+\frac{\Delta t}{r_c}\vec{\xi}$$

Finally, the stochastic force must be made dimensionless. By fluctuation-dissipation theory, $\vec{\xi}=\sqrt{\frac{2\mu k_bT}{\Delta t}}\tilde{\xi}$ if $\tilde{\xi}$ is given by a Gaussian random distribution with $\sigma^2=1$.

Hence the full form of the equation can be written with entirely dimensionless variables as:

$$\tilde{r}(t+\Delta t)=\tilde{r}(t)+\Delta\tilde{t}\tilde{F}_{n-h}+\frac{\Delta t}{r_c}\sqrt{\frac{2\mu k_bT}{\Delta t}}\tilde{\xi}$$

$$\boxed{\tilde{r}(t+\Delta t)=\tilde{r}(t)+\Delta\tilde{t}\tilde{F}_{n-h}+\sqrt{2\Delta\tilde{t}}\,\tilde{\xi}}$$

Note that a step size of $\Delta\tilde{t}=10^{-4}$, equivalent to $\sim5\times10^{-10}\,s$, was used in all simulations